

The ferroelectric field-effect transistor with negative capacitance

I. Luk'yanchuk,^{1,2} A. Razumnaya,^{3,2} A. Sené,¹ Y. Tikhonov,^{1,3} & V. M. Vinokur²

Integrating negative capacitance (NC) into the field-effect transistors promises to break fundamental limits of power dissipation known as Boltzmann tyranny. However, realization of the stable static negative capacitance in the non-transient regime without hysteresis remains a daunting task. Here we show that the failure to implement the NC stems from the lack of understanding that its origin is fundamentally related with the inevitable emergence of the domain state. We put forth an ingenious design for the ferroelectric domain-based field-effect transistor with the stable reversible static negative capacitance. Using dielectric coating of the ferroelectric capacitor enables the tunability of the negative capacitance improving tremendously the performance of the field-effect transistors.

Dimensional scalability of field effect transistors (FETs) has reached the Boltzmann tyranny limit because of their inability to handle the generated heat¹. To reduce the power dissipation of electronics beyond this fundamental limits, negative capacitance of capacitors comprising ferroelectric materials has been proposed as a solution². The FET with a negative-capacitance ferroelectric layer has gained an enormous attention of researchers^{3–12}. However, after impressive initial progress that has resulted in a rich lore massaging the aspects of technological benefits of the prospective stable static negative capacitance, the advancement in the field decelerated considerably. The lack of a clear self-consistent physical picture of the origin and mechanism of the stable static negative capacitance^{7,11–14} not only retarded the craved technological progress, but has led to numerous invalid fabrications and misleading claims⁹.

In this work, we put forth a foundational comprehensive mechanism of the NC in ferroelectrics demonstrating inevitable emergence of the NC due to formation of polarization domains. We establish a practical design of the stable and reversible NC FET based on the domain layout. The proposed device is tunable and downscales to the 2.5-5 nm technology node.

Figure 1 demonstrates the principles of integrating the ferroelectric layer with the NC into the FET and the crucial role of domain states. The performance of the FET is quantified by the so-called subthreshold swing $SS = (\partial(\log_{10}I_d)/\partial V_g)^{-1}$ that describes the response of the drain current I_d to the gate voltage V_g . The lower the value of the SS , the lower power the circuit consumes. In a basic bulk metal-insulator-semiconductor field-effect transistor (MIS FET), shown in Fig. 1a, which generalizes the MOSFET structure, the subthreshold swing is

$$SS = \overbrace{\frac{\partial V_s}{\partial(\log_{10}I_d)}}^{SS_b} \overbrace{\frac{\partial V_g}{\partial V_s}}^m, \quad m = 1 + \frac{C_s}{C_g} \quad (1)$$

Here is the first factor, SS_b presents the response of I_d to the voltage V_s at the conducting channel region and the second one, so-called body factor, m , characterizes the response of the voltage V_s to the applied voltage V_g . Figure 1a shows the equivalent electronic circuit where C_g and C_s correspond to the gate dielectric and semiconducting substrate capacitancies, respectively.

The fundamental constraint of the energy/power efficiency of the MIS FETs is the thermal injection of electrons over an energy barrier enabling drain current flow and thus preventing the reduction of the factor SS_b below the 60 mV dec⁻¹, because the body factor $m > 1$ at $C_g, C_s > 0$. To overcome this limitation, the FETs incorporating the NC into the design has been proposed². Indeed, replacing the gate dielectric by the layer with negative capacitance C_{NC} would make the body factor $m < 1$ thus decreasing the SS below the Boltzmann limit.

Ferroelectric materials appear as the best candidates for realizing negative capacitance in FETs². The emergence of the NC in a ferroelectric capacitor follows from the Landau double-well landscape of the capacitor energy W as a function of the applied charge Q ¹⁵ (blue line in Fig. 1b). The upward curvature of $W(Q)$ at small Q implies that the addition of a small charge to the ferroelectric capacitor plate, induces non-zero polarization and reduces its energy. Hence a negative value of the capacitance $C_{NC}^{-1} = d^2W/dQ^2$ (Supplementary Notes 1 and 2). However, a monodomain configuration is unstable against domain formation^{16–20} having the lower energy at given Q . The red line in Fig. 1b presents free energy for a ferroelectric capacitor comprising two domains. The instability towards domain formation in other systems, following from analytical (Supplementary Note 1) and numerical (Supplementary Note 3) calculations is discussed in details in Supplementary Note 4. Although the NC preserves in multidomain configuration^{16,21–23}, domain formation may trigger some undesired effects detrimental to realizing the NC FET. The domains cause inhomogeneous electric fields endangering the conducting channel in the most commonly discussed metal-ferroelectric-semiconducting (MFS) FETs (Fig. 1c). Moreover, the high absolute value of the NC cannot properly match either the semiconducting substrate of the MFS FETs having the pre-transitional (incipient) ferroelectric state^{5,24,25} or an additional dielectric layer¹⁰ (MFIS FETs, Fig. 1d, see Supplementary Note 4 for details).

Importantly, a lot of previous publications missed these precepts, having thus resulted in scientifically misleading statements and obscuring claims concerning the practical engineering of the NC FET. Past suggestions of the ferroelectric-based NC FETs were building on the concept of a monodomain state of the ferroelectric layer. However, an inevitable formation of the multidomain state, while conserving the effect of the NC requires a careful inspection of the feasibility of the proposed devices.

Here we build the NC FET overcoming the discussed stumbling stones and successfully harnessing in the negative capacitance. We integrate the MFM ferroelectric capacitor into the gate and architect the metal-ferroelectric-metal-dielectric-semiconductor (MFMIS) and coated c-MFMIS structures as shown in Fig. 1e,f. We spotlight that while such systems are yet unstable against the domain formation, they host, unlike the multidomain MFS and MFIS structures, precisely two domains separated by the domain wall^{23,26}. It is manipulating the domain wall by the applied charges that creates the NC effect²³ (Supplementary Note 5). Moreover, although the presence of two domains induces inhomogeneous electric fields, the electrodes level the inhomogeneity down and prevent the destruction of the conducting channel in the semiconducting substrate. The coating of the ferroelectric layer with the dielectric spacer in the c-MFMIS makes an extra capacitor parallel to C_{NC} . Such a design allows not only to establish the stable reversible NC but to vary and tune the NC parameters in a wide desirable range ensuring the proper match

¹University of Picardie, Laboratory of Condensed Matter Physics, Amiens, 80039, France; ²Terra Quantum AG, St. Gallerstrasse 16A, CH-9400 Rorschach, Switzerland. ³Faculty of Physics, Southern Federal University, 5 Zorge str., 344090 Rostov-on-Don, Russia.

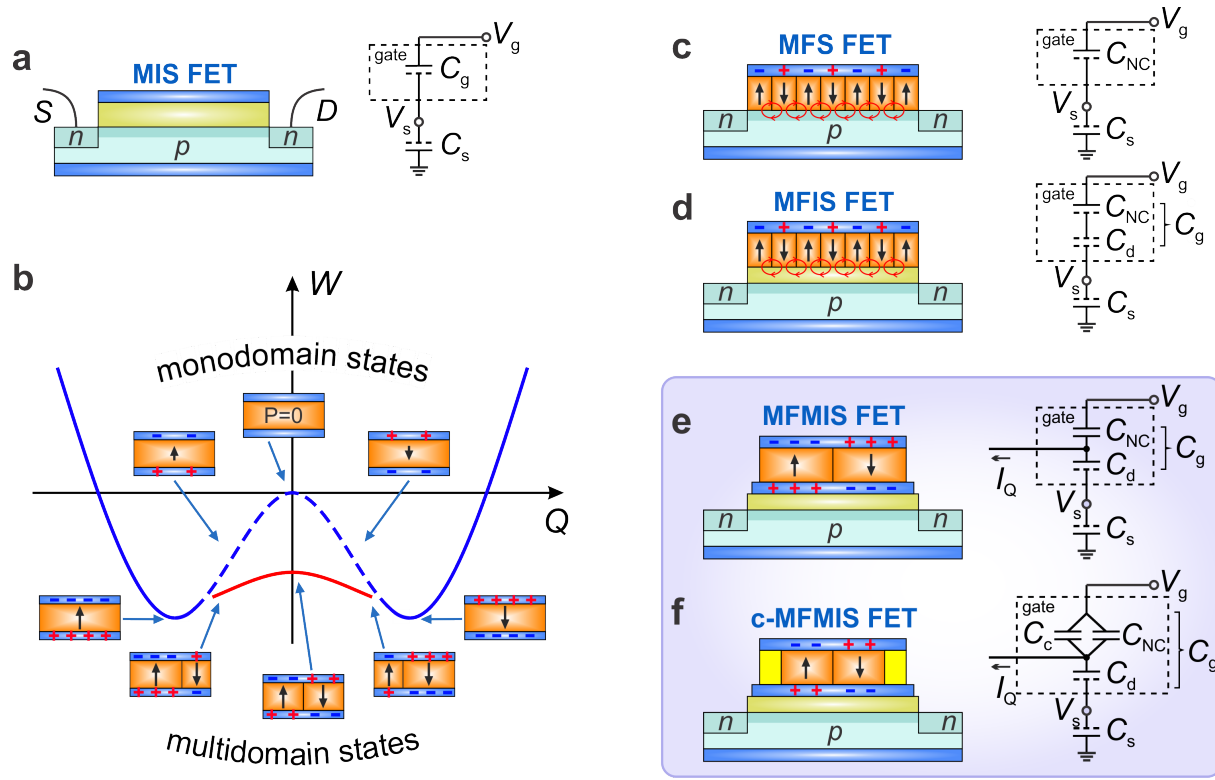


Fig. 1 | Stability and feasibility of the ferroelectric-based NC FETs. **a**, Bulk MIS FET. Pale blue: p-type semiconducting substrate; dusty blue: source (S) and drain (D) of n-doped regions connected by conducting channel; sky blue: bottom ground electrode. The gate stack: gate electrode and oxide gate dielectric layer (yellow green). Right: equivalent circuit comprising gate dielectric capacitance, C_g , and capacitance to the ground, C_s , of the substrate. Solid lines depict electrodes, dashed lines depict interfaces without electrodes; V_g is the applied gate voltage, V_s is the channel potential. **b**, The energy, W , and polarization states of the ferroelectric (orange) capacitor as a function of the driving charge Q . The unstable energy branch (dashed line) depicts the energy of the monodomain state. The energy of a stable two-domain state is shown by the red curve. Plus and minus signs show the distribution of charges at the plates. **c**, Multidomain structure of the MFS FET with redistributed electric charges at the top gate electrode and fringing electric fields (red loops) at the FS interface. Ferroelectric capacitance $C_{NC} < 0$ replaces $C_g > 0$ of the MIS FET. **d**, MFIS FET incorporates the dielectric layer with $C_d > 0$. **e**, MFMIS FET integrating a floating gate electrode into the MFIS FET between ferroelectric and dielectric layers. **f**, The coated c-MFMIS FET: the dielectric shell (yellow) with $C_c > 0$ coats the ferroelectric layer.

of the gate to the substrate.

Figure 2 presents a general design of MFMIS and c-MFMIS FETs and illustrates the domain-based functioning principles and performance characteristics. A three-dimensional view of the MFMIS FET which consists of the gate stack deposited over grounded semiconducting substrate with the source and drain parts connected by the gate-operated conducting channel, is presented in the panel (a). The nanodot-scale two-domain ferroelectric capacitor integrated into the gate stack is a major element enabling the NC response via the applied charge-controlled motion of the DW. The NC response arises since the length, hence the energy of the displacing DW is sensitive to the shape of a ferroelectric capacitor. To ensure the best controlled performance of the NC, we choose a disc-like form of a capacitor.

In the transistor design, the top electrode of the capacitor is the top gate electrode of the MFMIS FET connected to the external voltage source. The bottom electrode of the capacitor, stabilizing the ferroelectric two-domain state is an intermediate, electrically isolated floating gate electrode of the transistor that preserves the entire charge, most commonly a zero total charge, constant. Along the way, the floating gate resolves a frequent issue of neutralizing the parasitic charges that may be trapped by interfaces during the fabrication and functioning. Maintaining the working charge and providing a regular rubbing out the parasite leaking charges with the removal time faster than the leakage time²⁷

is achieved via the standard discharging methods, either harnessing the Fowler–Nordheim tunneling and the hot electrons injection²⁸, or circuiting the gate by the auxiliary charge-carrying current, I_Q , contact, see Fig. 1e,f to a certain source for a given combination of electric inputs ensuring the proper sequence of discharging and high resistance modes²⁹. The floating gate also makes the potential along the ferroelectric interface even, maintaining, therefore, a uniform electric field across the gate stack and substrate. The ferroelectric capacitor is attached to the substrate through the gate dielectric which is the high- κ insulating layer, preventing an uncontrolled charge leakage between the floating-gate electrode and the semiconducting channel.

An effective electronic circuit of the MFMIS FET, shown in Fig. 1e, is similar to that of the multidomain MFIS FET (Fig. 1d). The difference is that now the task of leveling the depolarization field inhomogeneities is taken by the floating gate electrode. Therefore, the gate dielectric layer can be safely engineered as utmostly ultrathin one, down to the technologically-acceptable limit of a few nanometers. This increases C_d with respect to $|C_{NC}|$, opening doors to making the gate capacitance negative, $C_g^{-1} = C_d^{-1} - |C_{NC}^{-1}| < 0$. Yet it is hard to achieve a required largeness of C_d with respect to $|C_{NC}|$ due to the restrictions imposed by materials compatible with the silicon CMOS technologies. To meet the challenge, we devise a coated c-MFMIS FET that critically changes the situation and breaks ground for the unlimited enhancement of the performance of

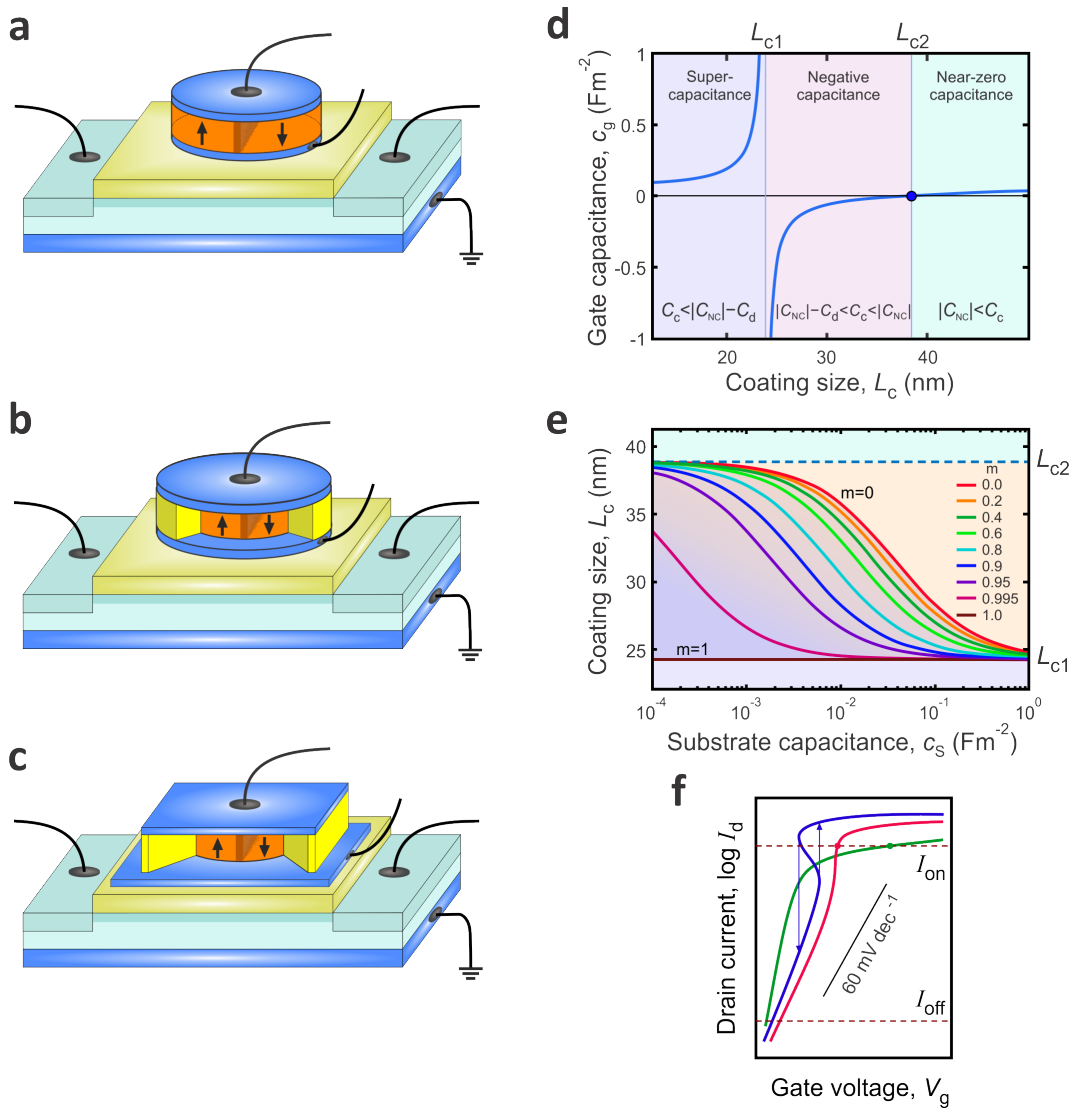


Fig. 2 | Functioning of the MFMS FET. **a**, A three-dimensional sketch of the MFMS FET comprising a disc-shape ferroelectric capacitor with the negative capacitance. **b**, A sketch of the coated MFMS FET, in which the ferroelectric disc is sheathed by the dielectric shell. The dielectric shell shares the top-gate and floating-gate electrodes with the ferroelectric disc, hence making a complimentary capacitor going in parallel with the ferroelectric capacitor. **c**, Rectangular modification of the c-MFMS FET. The extended area of coating and gate dielectric layer capacitors enhances the performance of the NC FET. **d**, Normalized gate capacitance c_g as function of the coating size L_c . Colored areas show three distinct regimes of the gate functioning. **e**, A set of $L_c(c_s, m)$ dependencies enabling us to determine the body factor m of the c-MFMS FET as function of the normalized substrate capacitance, c_s and coating size L_c . The working region is confined between curves corresponding $m = 0$ and $m = 1$. The instability region is colored in pink. The green and purple regions correspond to the super- and near-zero c_g areas of panel (d). **f**, Comparison of transport characteristics $I_d(V_g)$ of different c-MFMS FETs.

the NC FET transistor.

The coating the ferroelectric layer with the dielectric oxide sheath confined by the same electrodes, see Fig. 2b,c, straightforwardly incorporates an additional capacitor with the capacitance $C_c > 0$ in parallel to C_{NC} . This results in a radical improvement of the controlled tuning of the gate capacitance. In particular, manipulating with the sizes of the coating oxide layer and with the geometrical design of the device as a whole provides a broad variation in its performance characteristics and functioning regimes. The panels (b) and (c) exemplify possible designs. The panel (b) shows an annulus-like coating capacitor, while panel (c) displays a rectangular design of the coating layer and, in addition, the possibility of increasing the area of the floating gate electrode with respect to the top gate electrode. The latter design allows for controllable increasing capacitances of the coating and gate-dielectric layers most efficiently, maintaining the miniaturization of the device. Note that in all

the geometries the core ferroelectric should maintain its disc-like shape ensuring the optimal manipulation with the DW.

Shown in Fig. 1f is the equivalent circuit of c-MFIS FET. The important advance is that the gate capacitance becomes

$$C_g = \frac{1}{C_d^{-1} + (C_c - |C_{NC}|)^{-1}}, \quad (2)$$

which permits tuning C_g over the widest range of values by the appropriate modifying the parameters of the coating capacitor. We reveal the rich dependence of C_g on the coating layer size, L_c choosing the rectangular geometry of the coating layer (Fig. 2c). The capacitance of the disk-shape two-domain ferroelectric capacitor given in²³, is

$$C_{NC} = -\epsilon_0 \epsilon_f \frac{S_f}{d_f} \gamma \frac{D_f}{\xi_0}. \quad (3)$$

The capacitances of the coating and gate dielectric layers are taken in a standard form as $C_c = \epsilon_0 \epsilon_c S_c / d_c$ and $C_d = \epsilon_0 \epsilon_d S_d / d_d$, respectively. Here $S_f = \pi D_f^2 / 4$, $S_c = L_c^2 - S_f$ and $S_d = L_d^2$ are areas of the ferroelectric, coating dielectric and gate dielectric plate surfaces, respectively, $\gamma \approx 4.24$ is a numerical factor accounting for the energy of the bent DW and ϵ_0 is the vacuum permittivity and $\xi_0 \approx 1\text{nm}$ is the thickness of the DW.

The behavior of C_g defined by Eq. (2) is most generic and does not depend critically on the specific choice of materials. For practical applications, we choose both, the coating layer and the gate-dielectric layer, be composed of the Si-compatible dielectric HfO_2 with the respective dielectric constants ϵ_c , ϵ_d being approximately equal to 25. The ferroelectric disc of the diameter $D_f \approx 6\text{nm}$ and thickness $d_f \approx 3\text{nm}$, may be fabricated out of the ferroelectric phase of HfO_2 or its Zr-based modification, $\text{Hf}_{0.5}\text{Zr}_{0.5}\text{O}_2$ with $\epsilon_f \approx 50$ ¹³. In fact, ϵ_f is the only relevant parameter that defines the NC properties of two-domain ferroelectric layer; therefore, the consideration applies equally well to other similar ferroelectrics, for instance, to perovskite oxides, like strained PbTiO_3 (see Supplementary Notes 1 and 5). The height of the gate dielectric layer is taken as $d_d \approx 3\text{nm}$, whereas the thickness of the coating layer, d_c , is equal to d_f . The size of the rectangular floating-gate electrode, L_d , defining the size of the gate dielectric capacitor, is taken as $1.2L_c$.

Figure 2d displays the derived normalized gate capacitance, $c_g = C_g / S_d$ as function of L_c and shows the three distinct regimes of the gate functioning set by two critical sizes, $L_{c1} < L_{c2}$, of the coating layer: (i) the super-capacitance, $L_c < L_{c1}$, (ii) the negative-capacitance, $L_{c1} < L_c < L_{c2}$, and (iii) the near-zero capacitance, $L_{c2} < L_c$, regimes. All three regimes are of tremendous relevance for applications. We restrict ourselves to the detailed analysis of the NC regime, leaving the detailed discussion of regimes (i) and (iii) to forthcoming publication.

An unrestricted range of variation of c_g , from minus infinity to zero, as seen from Fig. 2d, allows for the unlimited tuning of the magnitude of the gate NC. In particular, the possibility of making it arbitrary small, enables us to overcome an insurmountable obstacle of the proper matching between the gate and substrate capacitancies and obtain any predefined value of the body factor, $0 < m < 1$, getting thus the remarkably low values of SS , the task not achievable by previously suggested architectures. To optimize the parameters, we relate L_c and the normalized substrate capacitance $c_s = C_s / S_d$ to different m as shown in Fig. 2e for our exemplary c-MFMIS FET.

$$m = 1 + \frac{C_s}{C_g} = 1 + \frac{C_s}{C_d} + \frac{C_s}{C_c - |C_{\text{NC}}|}, \quad (4)$$

The $L_c(c_s, m)$ curves standing for $m = 0$ (red) and $m = 1$ (brown), confine the stable working interval for the c-MFMIS FET. The region below the brown line where $m > 1$, i.e., $SS > 60\text{ mV dec}^{-1}$ corresponds to the small sizes of the coating layer, $L_c < L_{c1}$. The region above the $m = 0$ curve but below the $L_c = L_{c2}$ line is the hysteretic loss of the reversibility region. Therefore, the proper choice of L_c , in the interval $L_{c1} < L_c < L_{c2}$, enables the desired magnitude of m for a given value of the substrate capacitance c_s . Although in our model example, the lateral size of the coating layer varies between $L_{c1} \approx 24$ and $L_{c2} \approx 38\text{ nm}$, it can be significantly further reduced down to practically the diameter of the ferroelectric disc, by increasing the dielectric constant of the coating material by factor of four.

Moreover, the established dependence $L_c(c_s, m)$ for c-MFMIS FET (Fig. 2e) enables us to meet the critical challenge of the NC FET performance, spelled out in⁹. Namely, how to properly match the highly nonlinear voltage-dependent C_s , which dramatically increases, typically by the order of magnitude, from the capacitance of the depletion layer to the quantum capacitance of the channel with injected conducting electrons. The optimal regime for exemplary system which keeps the steep slope of the $I_d(V_g)$ dependence over the entire voltage working range that includes not only the subthreshold, but also near- and above threshold regimes, preserving the stable and hysteresis free $I-V_g$ transfer characteristics at the same time is shown in Fig. 2f by the red line. The green and blue curves show the $I_d(V_g)$ dependencies for transistors with the steeper SS

having the voltage-independent (green) and nonlinear in voltage (blue) substrate capacitancies. The procedure, detailed in Supplementary Note 5 describes the calculations and constructing the minimal gate model, accounting for the $V_g(Q_g)$ and $C_s(V_s)$ nonlinear dependencies, to incorporate the working characteristics of c-MFMIS FET into the process designer kit (PDK) to accomplish a practical breakthrough in the transistor performance development.

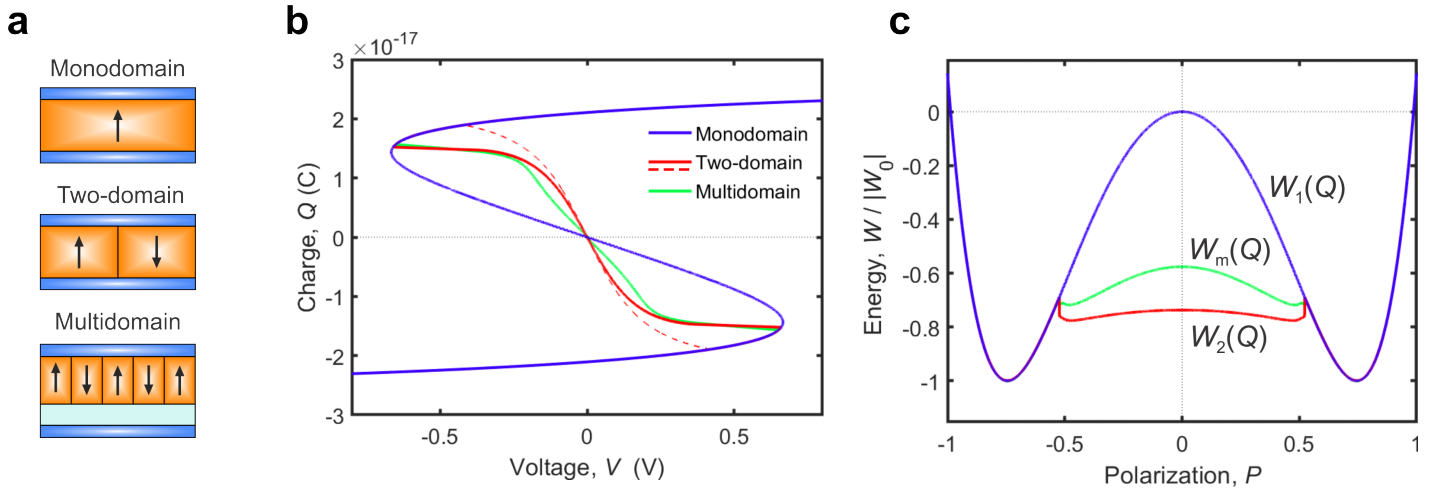
The achieved understanding that the fundamental mechanisms of the NC is the domain action, bestows closing the gap between the concept of the ferroelectric negative capacitance and its realization in electronic devices. It enables designing a stable NC-based FET, whose coating-shell architecture of the gate promises to bring forth an unprecedented performance and high tunability of characteristics allowing the perfect match with advanced FET architectures. Our findings lay out the way for scaling the NC FET nanoelectronics down to 2.5-5 nm technology nodes via utilizing the CMOS-compatible ultra-thin and ultra-small ferroelectric disc as a core of the NC gate.

Supplementary Note 1: Ferroelectric capacitors, negative capacitance and energy

In this Supplementary Note we present the analysis of the onset of the NC in the charge-controlled monodomain ferroelectric capacitor and demonstrate the instability of a monodomain state against the multi-domain formation in the capacitors with the metal-ferroelectric-metal (MFM) and metal-ferroelectric-semiconductor-metal (MFSM) layer configurations. The electrodynamic properties of the MFSM setup with the depleted semiconducting layer are equivalent to those in the metal-ferroelectric-insulator-metal (MFIM) configuration, and the approach developed in Refs. [17–19, 22–24] is to be applied. The investigated setups are sketched in Fig. S1a. Figure S1b demonstrates the charge-voltage, $Q-V$, characteristics of these capacitors. The details of calculations and numerical simulations are given in the subsequent Supplementary Notes. Figure S1c shows the respective energy profiles, which clearly demonstrate that the monodomain energy branch, $W_1(Q)$ is always higher than those for the two-domain state, $W_2(Q)$, in MFM capacitor and for the multidomain state, $W_m(Q)$, in MFSM capacitor. Hence, in either case the monodomain system is always unstable towards the emergence of domains.

The existence of the NC in a single-domain ferroelectric capacitor follows from the double-well landscape of the capacitor energy W as a function of the applied charge Q [15], (blue line in Fig. S1c), inherited from the Landau free energy polarization dependence $F(P)$ in ferroelectrics (see Supplementary Note 2 for detailed derivation). The upward curvature of $W_1(Q)$ at small Q corresponding to the incipient ferroelectric state with $P = 0$ at $Q = 0$ implies that the addition of a small charge to the ferroelectric capacitor plate, induces non-zero polarization and reduces its energy. Hence a negative value of the capacitance $C_{\text{NC}}^{-1} = d^2 W_1 / dQ^2$. The stability of the NC effect rests on the design ensuring that it is the charge that controls the state of the capacitor [5]. Had one allowed for the charge to vary freely, for example, by short-circuiting the capacitor's plates, the system would have fallen into one of the energy minima corresponding to the spontaneously polarized states. The in-series capacitance circuit of the NC FET, shown in Fig. 1a, in which C_g is replaced by $C_{\text{NC}} < 0$, sets in the required charge-controlled operational mode. The controlling charge is set by the gate voltage, V_g , as $Q = C_{\text{FET}} V_g$, where $C_{\text{FET}}^{-1} = C_s^{-1} - |C_{\text{NC}}^{-1}|$ is the total capacitance of the transistor. This mode is stable and reversible as long as C_{FET} remains positive, ensuring condition $m > 0$ required for the stability of the circuit.

The above consideration pertains to a single-domain configuration which is widely used to explain the NC of the ferroelectric layer integrated into the FET. However, as follows from the fundamental thermodynamics consideration, the homogeneous phase with $P = 0$, corresponding to the maximum of the energy landscape at $Q = 0$, is unstable with respect to the spinodal decomposition into the mixture of phases with oppositely oriented polarization. This mixture possessing the lower energy is a texture of the oppositely oriented ferroelectric domains. Im-



Supplementary Figure 1 | The characteristics of the different types of the ferroelectric capacitors. **a**, The sketches of the domain configurations in a ferroelectric layer of MFM and MFIM capacitors. From top to bottom: monodomain, two-domain and multidomain states, respectively. **b**, The charge-voltage characteristics, Q - V , of the monodomain and two-domain states of the MFM capacitors (the so-called S-curves) are shown by blue and red solid lines, respectively. The red dashed line corresponds to the analytical approximation for the Q - V dependence in the two-domain state. The lime line shows the Q - V characteristic of the multidomain state in a ferroelectric layer for the MFIM capacitor. **c**, The double-well energy profile of the ferroelectric capacitors as function of the applied charge. The colour scheme corresponds to the states in the panel (b). In case of the MFIM capacitor, only the energy fraction corresponding to the ferroelectric layer is shown. It is clearly seen that the monodomain state with energy $W_1(Q)$ is unstable against the formation of either two-domain state in the MFM capacitor with $W_2(Q)$ or the multidomain state in MFIM capacitor with $W_m(Q)$ at the fixed charge Q . The energy is normalized on the absolute value of the energy of the monodomain short-circuited ferroelectric capacitor, $|W_0|$.

portantly, the integral phase-controlling parameter, which is the charge Q at the electrodes in our case, conserves upon the decomposition. The structural details of the formed coarse-grained phase texture, modeled by the phase-field method (Supplementary Note 3) depend on the interaction with the external environment.

Supplementary Table I summarizes the results of the analytical estimates of the negative capacitancies and energies of the tested systems, derived using the NC theory [22, 23]. These results are remarkably close to those, obtained from the simulations, which confirms the robustness of the calculations and again demonstrates an instability of the monodomain system against the domain emergence. In Supplementary Table I and in the subsequent calculations, the capacitance, $C_f = \epsilon_0 \epsilon_f \frac{S_f}{d_f}$ and the energy, $W_0 \approx -S_f d_f P_0^2 / (8\epsilon_0 \epsilon_f)$ of the ferroelectric capacitor in the stable monodomain polarization state with $P = P_0$, are used as the normalization parameters. The other parameters are defined as follows: S_f and d_f are the capacitor area and thickness ($S_f = \pi D^2/4$ in case of the disk-shape capacitor with the diameter D), ϵ_0 and ϵ_f are the vacuum permittivity and longitudinal (along P) ferroelectric dielectric constant, $\kappa = (\epsilon_f / \epsilon_{f\perp})^{1/2}$ is the anisotropy of the dielectric tensor (where $\epsilon_{f\perp}$ is the transversal dielectric constant; in Ref. [22] ϵ_f and $\epsilon_{f\perp}$ were denoted as ϵ_{\parallel} and ϵ_{\perp} respectively); w is the domain width in the multidomain texture, γ_1 depends on the polynomial type of the Ginzburg-Landau energy expansion and typically varies between 2 and 3, $\gamma_2 = \frac{4}{3\nu} \approx 4.24$ (with $\nu \approx 0.1$) and $\gamma_m = \frac{\pi}{4\ln 2} \frac{\xi}{\kappa} \approx 4.55$ are the numerical factors accounting for the specific geometry and energetics of the DWs in the two- and multidomain case, ξ_0 is the characteristic thickness of the DW, and ζ is the factor, reflect-

ing the interface boundary conditions. In our case of the MFIM setup $\zeta = 2(1 + \epsilon_s / (\epsilon_f \epsilon_{f\perp}))^{1/2}$. The numerical estimation in the Supplementary Table I are given for our model cases with $d_f = 3$ nm, $D = 6$ nm, $\xi_0 \approx 1$ nm, $w \approx 3$ nm. The dielectric parameters, $\epsilon_f = 50$, $\epsilon_s = 25$, $\kappa = 1$, $\zeta \approx 4$, are selected to be close to those used for the conventional ferroelectric FETs with high- κ gate dielectric and either PbTiO_3 or HfO_2 -based ferroelectric materials.

Supplementary Note 2: Instability of the monodomain state

The emergence of the spontaneous polarization, P , in uniaxial ferroelectric and its interaction with the electric field, E , is conventionally described by the free energy functional

$$F = \int (F_{\text{GL}}(P) - EP) dV, \quad (\text{S1})$$

where the zero-field Ginzburg-Landau free energy is

$$F_{\text{GL}}(P) = aP^2 + bP^4 + cP^6. \quad (\text{S2})$$

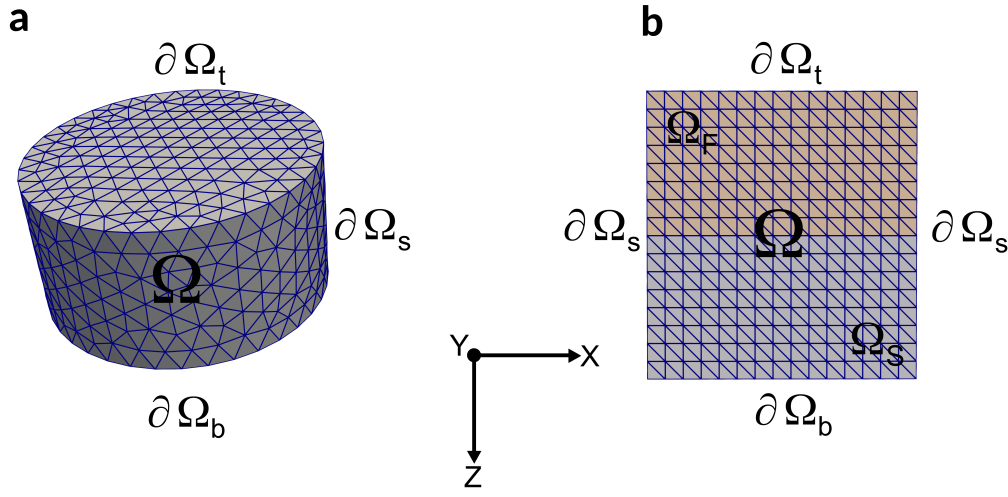
For illustration purposes we take the Landau coefficients, $a = -0.2954$, $b = 0.05$, $c = 0.26$ corresponding to the substrate-strained PbTiO_3 at $T = 25^\circ\text{C}$ with the compressive strain -1.3% [30].

The minimization of the Eq. (S1) with respect to P ,

$$\frac{\delta F}{\delta P} = 2aP + 4bP^3 + 6cP^5 - E = 0, \quad (\text{S3})$$

Type of capacitor	Capacitance, NC	Energy at $Q = 0$	Reference
MFM monodomain (unstable)	$C_1 = -\gamma_1 C_f \approx -2 C_f$	$W_1 = 0$	
MFM two-domain (stable)	$C_2 = -\gamma_2 \frac{D}{\xi_0} C_f \approx -25.4 C_f$	$W_2 / W_0 = -1 + \frac{64\nu \xi_0}{\pi D} \approx -0.66$	[23]
MFIM multidomain (stable)	$C_m = -\gamma_m \frac{d_f}{w} C_f \approx -4.55 C_f$	$W_m / W_0 = -1 + \frac{7\zeta(3)}{\pi^3} \frac{\xi}{\kappa} \frac{w}{d_f} \approx -0.46$	[22]

Supplementary Table I



Supplementary Figure 2 | Finite-element meshes. **a**, Cylindrical mesh used for two-domain simulations in MFM setup. **b**, Front-side view of rectangular mesh used for multi-domain simulations in MFSM setup.

implicitly defines the constitutive relation $P = P(E)$ which is a basic relation defining the electrodynamics of ferroelectric.

Adjusting Eq. (S1) to the ferroelectric capacitor MFM setup, yields the polarization-voltage relation for the monodomain MFM system

$$V(P) = -d_f E = -d_f (2aP + 4bP^3 + 6cP^5). \quad (\text{S4})$$

In case of the capacitor, controlled by the charge Q , Eq. (S4) should be completed by the electrostatic boundary conditions at the capacitor electrodes which are electrically isolated from the external source:

$$-Q(P) = S_f (P + \varepsilon_0 \varepsilon_i E(P)) = S_f \left(P - \varepsilon_0 \varepsilon_i \frac{V(P)}{d_f} \right). \quad (\text{S5})$$

Here $S_f = \pi D_f^2/4$ and d_f are the area and thickness of the disc-shape capacitor of diameter D_f , ε_0 is the vacuum permittivity and $\varepsilon_i \approx 10$ is the background dielectric constant of the ferroelectric provided by the displacement of the non-polar ions. In coherence with the cylinder geometry of NC FET considered in the article, we take $D_f \approx 6\text{nm}$ and $d_f \approx 3\text{nm}$.

Equations (S4) and (S5) parametrically define the presented in Fig. S1b nonlinear Q - V characteristics of the monodomain transistor (where P is the running parameter) that is similar to the S-shape of the $P(E)$ constitutive relation of bulk uniform ferroelectric. Accordingly, the energy of the charge-driven monodomain capacitor is

$$W_1 = \int V dQ = S_f d_f F_{\text{GL}}(P) + \frac{1}{2} \varepsilon_0 \varepsilon_i \frac{S_f}{d_f} V^2(P). \quad (\text{S6})$$

The corresponding energy of the ferroelectric layer is displayed in Fig. S1c as function of the capacitor charge, Q ; using the $Q = Q(P)$ relation (S5) it acquires a double-well profile, identical to that of the Landau double-minima potential (S2). The maximum of $W_1(Q_1)$ corresponds to the paraelectric phase with $V, Q = 0$ and the two degenerate minima describe the states with $V = 0$ and $\pm Q_0 = \pm S_f P_0$ where $\pm P_0$ are the stable polarization states of a uniform short-circuited ferroelectric slab given by the minima of Eq. (S2). As follows from Fig. S1c, the monodomain energy branch, $W_1(Q)$ lies higher than two- and multidomain branches $W_2(Q)$ and $W_m(Q)$ for the two-domain MFMIS, and multi-domain MFS and MFIS realization of FETs.

- Hence, the monodomain state is unstable against domain formation, making the monodomain implementation of NC FET impossible.

We establish this instability employing an exemplary setup of the MFM capacitor with the charge-controlled electrodes [23, 26]. There,

an incipient state $P = 0$ at $Q = 0$ is unstable towards the formation of a state comprising two domains of equal cross-section areas, having alternating-directed polarization, and separated by the domain wall (DW). The charges at the electrodes evenly redistribute in order to screen the depolarization charges emerging at the ferroelectric's surfaces (keeping the total controlling charge $Q = 0$) and thus to reduce the electrostatic energy of the system. Indeed, the energy cost to create a DW with the appropriate redistribution the charges over the electrodes is much less than the energy necessary to eliminate the polarization over the whole sample for creating the zero-polarized incipient state while maintaining the zero charge density at the electrodes.

Tuning the controlling charge displaces the DW from its equilibrium position, see Fig. 1b of the main text. At some threshold value of the applied charge, when it becomes equal to the depolarization charge of the uniformly oriented polarization, the DW reaches the edge of a ferroelectric layer and the single-domain state restores. Therefore, the energy of the system decreases with the application of the charge from the energy of the two-domain state at $Q = 0$ to the energy single-domain uniformly polarized state that forms as the DW leaves the sample. The resulting $W_2(Q)$ dependence (Fig. S1c) displays the hump at $Q = 0$, hence, since the condition $C_{\text{NC}}^{-1} = d^2 W_1/dQ^2 < 0$ maintains, the NC persists. Importantly, the branch $W_2(Q)$ locates lower than the branch $W_1(Q)$ standing for the unstable uniformly-polarized scenario of the NC. Contrary to the prevailing opinion [6] the corresponding S-shape Q - V curve for the domain state (Fig. S1b) is well defined and pretty measurable experimentally.

The instability of the monodomain state in the MFIM capacitor against the emergence of the multidomain states is discussed in the subsequent Supplementary Notes.

Supplementary Note 3: Phase-field simulations

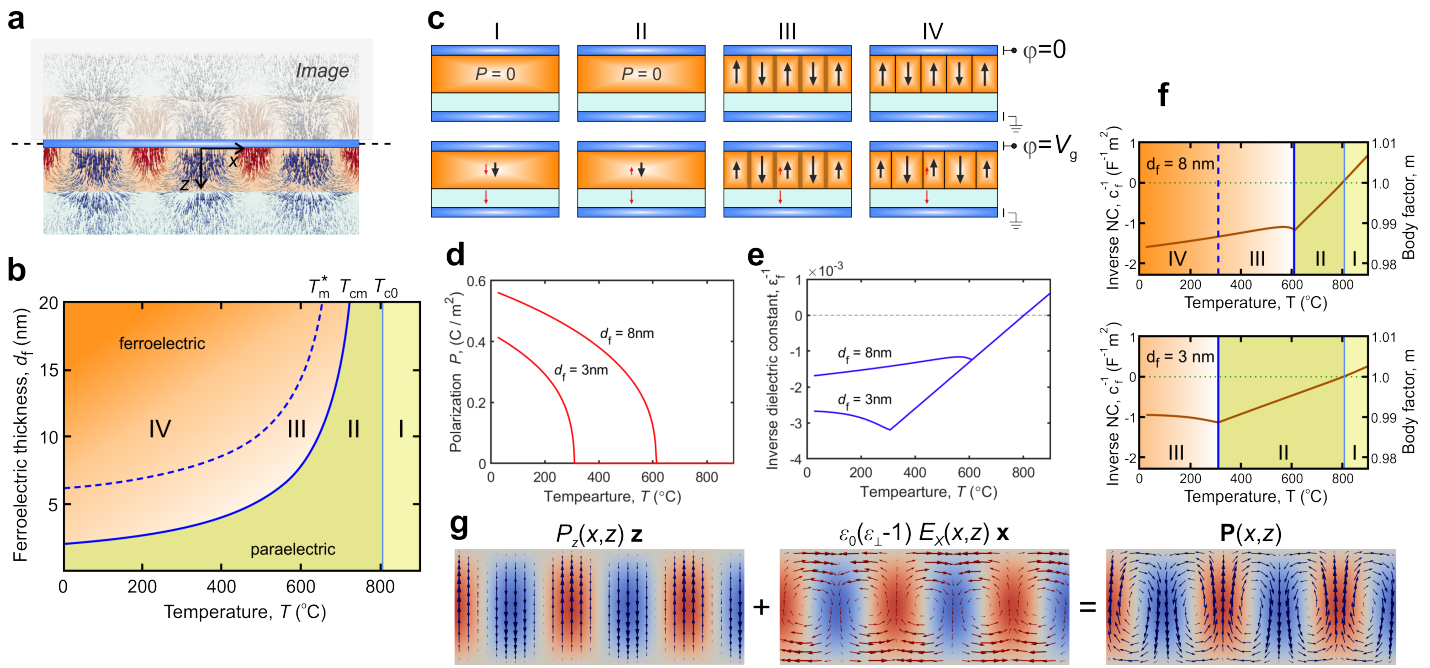
To carry out the phase-field simulations to calculate properties of two- and multidomain states we have used the open-source FEniCS computing platform [31]. The partial differential equations to solve result from the variation of the free energy functional F with respect to the polarization variable \mathbf{P}

$$-\gamma \frac{\partial \mathbf{P}}{\partial t} = \frac{\delta F}{\delta \mathbf{P}}. \quad (\text{S7})$$

To account for the electrostatics, these equations need to be completed by the Poisson equation

$$\varepsilon_0 \varepsilon_i \nabla^2 \varphi = \nabla \cdot \mathbf{P}, \quad (\text{S8})$$

where φ is the electric potential and $\varepsilon_i \approx 10$ is the background dielectric constant of the non-polar ions. The actual form of F for the model fer-



Supplementary Figure 3 | Multidomain state in the MFS FET. **a**, The lower part of the panel, below the dashed line, exhibits the polarization distribution in the up (red arrows) and down (blue arrows) oriented domains in the ferroelectric (orange) and semiconducting (pale blue) layers of the MFS FET, located below the metallic (sky blue) electrode. The upper part of the panel displays an image of the fictitious graphic continuation of the system, visualising its reflection in the metallic electrode. It is seen that the whole, the system and its image, is effectively equivalent to the IFI heterostructure. **b**, The d_f - T phase diagram of the MFS FET comprising four states having distinct dielectric properties: I denotes the paraelectric state, II is the incipient ferroelectric state, III is the soft-domain ferroelectric state, and IV is the hard domain ferroelectric state. **c**, The response of the ferroelectric states I-IV to the applied gate voltage, V_g . The states I and II maintain the paraelectric phase with $P = 0$ at zero voltage. Applied finite voltage induces the nonzero uniform polarization, shown by black arrow, and the internal electric fields in the ferroelectric and semiconducting layers shown by red arrows. Importantly, the direction of the electric field in the ferroelectric layer in the incipient ferroelectric phase II is opposite to the applied voltage, which is manifestation of the negative capacitance (NC) effect. The inverse direction of the electric field in ferroelectric layer, hence the NC effect, maintain in the soft-domain (III) and in hard-domain (IV) phases (only the average electric field is shown). The alternative change of the domains polarization amplitude (phase III and IV) and motion of the domain walls (phase IV) cause the NC dielectric response. **d**, The temperature dependence of the average polarization amplitude, P , for the multidomain ferroelectric layers of thickness $d_f = 3$ nm and $d_f = 8$ nm in MFS FET. **e**, The temperature dependence of the inverse dielectric constant, ϵ_f^{-1} , for the same multidomain ferroelectric layers of different thicknesses. Importantly, ϵ_f^{-1} is negative at temperatures below the bulk critical temperature T_{c0} . **f**, The temperature dependence of the inverse of the area-normalized capacitance, c_f^{-1} , for the same multidomain ferroelectric layers of different thicknesses and of the corresponding body factors of the respective MFS FETs with the capacitance of the semiconducting layer $c_s = 0.01$ F/m². The colored regions correspond to different ferroelectric states, shown in panel (c). **g**, In the soft multidomain state in ferroelectric slab the gradually distributed spontaneous z -directed polarization, $P_z(x, z)\mathbf{z}$ (left) produces the electric depolarization field, which is mostly oriented in the plane of the ferroelectric layer. This field triggers the induced polarization $\epsilon_0(\epsilon_{\perp} - 1)E_x(x, z)\mathbf{x}$ (middle). The superposition of the induced polarization and spontaneous polarization yields the vortex-like polarization texture $\mathbf{P}(x, z)$ (right). $P_z(x, z)\mathbf{z} + \epsilon_0(\epsilon_{\perp} - 1)E_x(x, z)\mathbf{x} = \mathbf{P}(x, z)$.

roelectric material, strained PbTiO₃, is defined for the MFM [23] and MFSM [32] simulation setups. The parameter γ determines the time scale for computations, its value, irrelevant for the static case, is taken equal to unity.

To create the finite-element meshes we used an open-source 3D mesh generator gmsh [33]. For the case of the two-domains simulations in MFM capacitor, the computational region at Fig. S2a is cylindrical volume Ω with $\partial\Omega_s$ being the side boundary of the cylinder and $\partial\Omega_t$, $\partial\Omega_b$ being the top and bottom boundaries of the cylinder, respectively. For the case of the multi-domains simulation in MFSM system, the computational region at Fig. S2b is rectangular volume Ω , where Ω_F is a ferroelectric part of the volume Ω and Ω_S is a semiconducting part of the volume Ω . The boundaries of the region are defined as follows: $\partial\Omega_s$ is the side boundary of the rectangular volume that consists of the left, right, front and back sides, $\partial\Omega_t$ is the top boundary of Ω_S and $\partial\Omega_b$ is bottom boundary of Ω_F . Meshes for both, MFM and MFSM cases, consist of the tetrahedral elements.

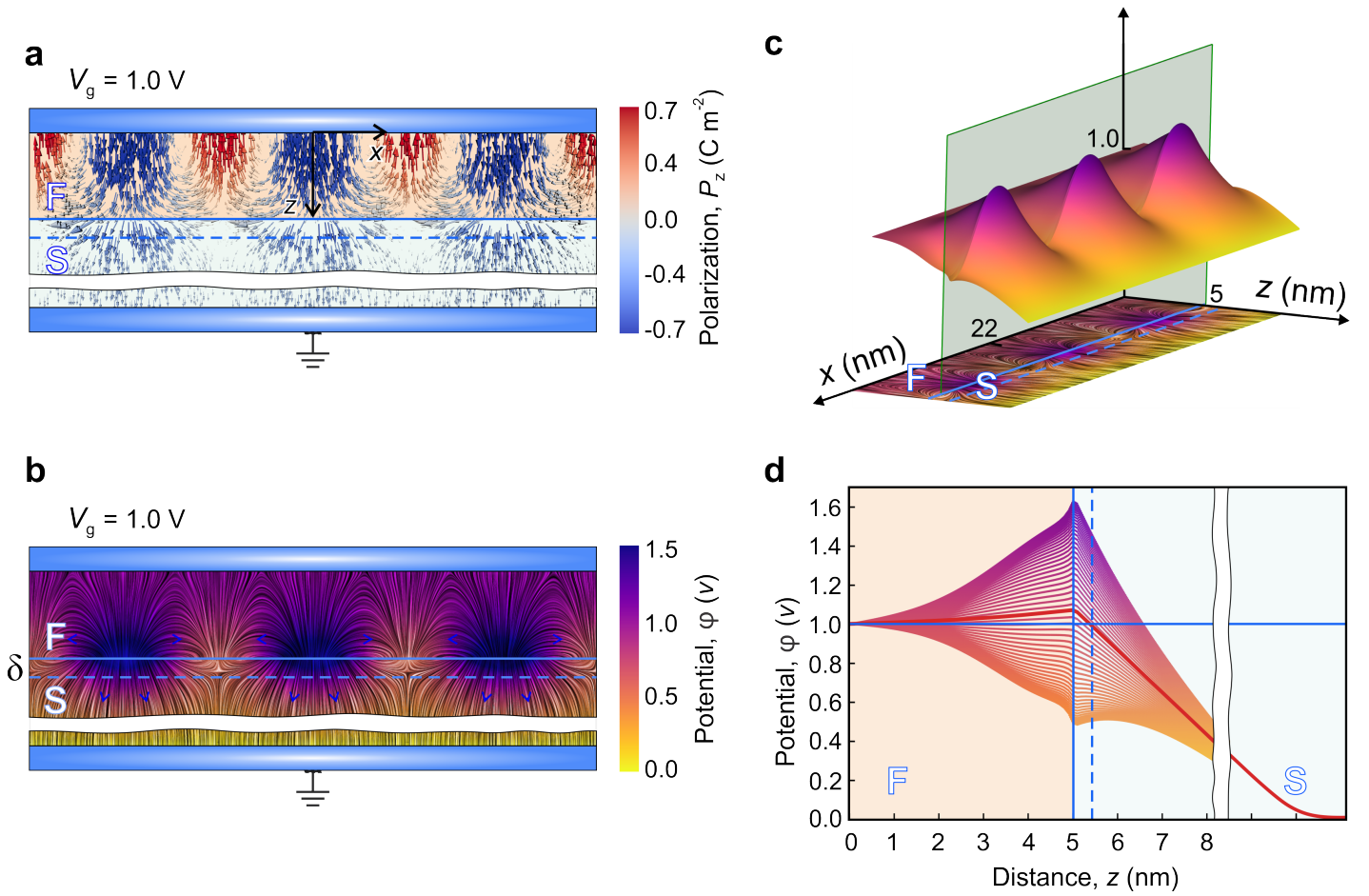
The solution for the polarization \mathbf{P} and electrical potential φ was sought in the functional space of the piece-wise linear polynomials. For simulation of the two-domain structure boundary conditions for \mathbf{P} on $\partial\Omega_s$, $\partial\Omega_t$ and $\partial\Omega_b$ of cylinder were free. However the equipotentiality and fixed total charge as an additional constraint were maintained at $\partial\Omega_t$ and $\partial\Omega_b$. The boundary conditions for \mathbf{P} and φ used in the simulation of the multi-domain structure were periodic in the x direction, to correctly

describe the periodicity of the emerging domain structure. This period, corresponding to the dimension of the rectangular volume Ω in the x direction was considered as an energy-minimizing parameter which was optimized for each series of calculations. Boundary conditions for \mathbf{P} on $\partial\Omega_t$ and $\partial\Omega_b$ as well as on the front- and back surface boundaries of the rectangular volume were free. The Dirichlet boundary conditions were imposed on φ , $\varphi(\partial\Omega_b) = 0$, $\varphi(\partial\Omega_t) = U$, where U is the applied voltage. The details of simulations are given in Refs. [23, 32].

To approximate the time derivative on the left hand side of Eq. (S7), we used the variable time BDF2 stepper [35]. Initial conditions for both, two-domain and multi-domain, simulations were the random distribution of \mathbf{P} vector components in the range of -10^{-6} - 10^{-6} C/m² at the first time step of simulation. The system of the non-linear equations arising from the discretization of Eq. (S7) was solved using the Newton based nonlinear solver with line search and generalized minimal residual method with the restart [36, 37]. On the each time step of the multi-domain simulation, linear system arising from discretization of Eq. (S8) was solved separately using a generalized minimal residual method with restart.

Supplementary Note 4: Pitfalls of MFS and MFIS FETs related to the emergence of domains

Although the NC effect has already been experimentally demonstrated in the dielectric-insulator superlattices [21] and although the MFS



Supplementary Figure 4 | The fields distribution in the multidomain state of the MFS FET under the applied gate bias. The potential $\varphi_0 = 1.0\text{ V}$ is applied to the top gate electrode. The bottom electrode is grounded. The region of the conducting channel is marked by the dashed line. **a**, The distribution of polarization in domains in the ferroelectric (F) layer is highly nonuniform. This non-uniformity extends even over the semiconducting (S) layer, disturbing the near-channel region. An applied electric field induces the non-zero average polarization by favoring the domains oriented along the field. However, the domain polarization dispersion still exceeds the average polarization value. **b**, The electric potential and electrostatic field lines in the ferroelectric and semiconducting channel regions are highly nonuniform, similarly to the polarization distribution. **c**, The 3D plot of the nonuniform electric potential distribution induced by the ferroelectric domains at the FS interface. **d**, The average potential distribution (red line) across the capacitor and the domain-induced potential scatter. The average potential enhancement at the FS interface and at the near-channel region with respect to the applied $\varphi_0 = 1.0\text{ V}$ corresponds to the NC effect. However, the scattering in the potential in this region substantially exceeds the potential enhancement that perturbs the conductivity channel, making the MFS configuration of the NC FET impractical. (The images are produced with Surface LIC toolbox in data visualisation application Paraview [34])

and MFIS gate stacks are being considered as most promising candidates for the NC applications [10], we show here that these structures can hardly be utilized for building the NC FET in practice. The major difficulty is the already mentioned destabilizing action of the depolarization fields, produced by the depolarization charges arising at the FI and FS interfaces that results in compulsory formation of the nonuniform domain texture. Although the domain structure keeps the collective NC effect [22], **two important offshoots inhibit its practical implementation in the MFS and MFIS FET.** Those are:

- The nonuniform field distribution disturbs the conducting channel formation in vicinity of FS interface.
- The high absolute value of the NC cannot properly match with the semiconducting substrate.

To bury the structures having these pitfalls on the quantitative basis, we note that the electrode-ferroelectric interface is described by the electrostatic equipotential boundary condition, hence the MFS system is equivalent to the dielectric-ferroelectric-dielectric (IFI) heterostructure in which the thickness of the ferroelectric layer is doubled, as shown in panel (a) of Fig. S3, and the electrostatic properties of dielectric layers are described by the dielectric constant of the depleted region of semiconductor, ϵ_s . This mapping allows us to use the results and calculation

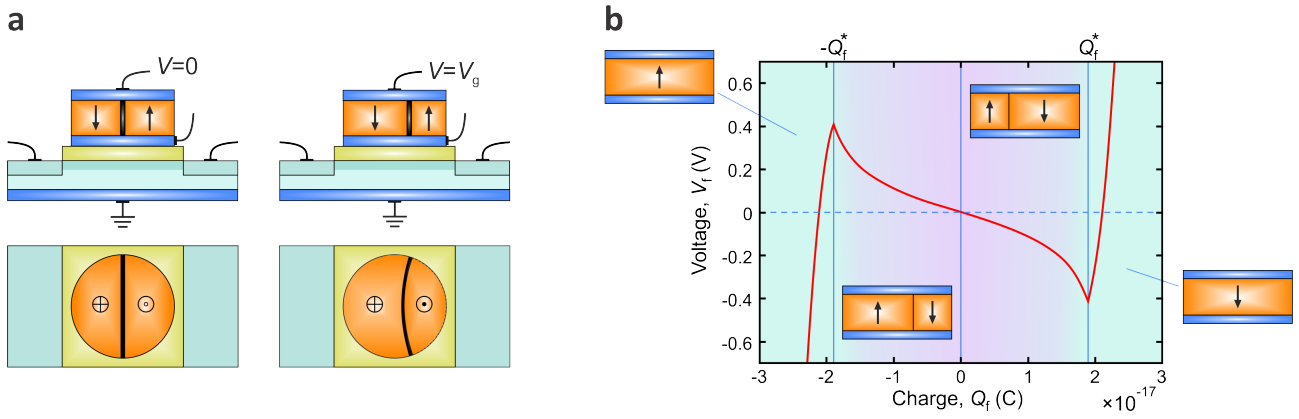
techniques developed in [17–19] for the IFI heterostructures and compare them with results of the phase-field simulations described in Supplementary Note 3.

Deriving from the results of [17–19] we note, first, that the transition temperature to the multidomain ferroelectric state of MFSM structure, T_{cm} , is lower than that for the monodomain bulk sample with the short-circuited electrodes, T_{c0} , and is given by

$$T_{cm} = \left(1 - 2\pi \left(\frac{C_{Curie}}{T_{c0}\epsilon_{\perp}} \right)^{1/2} \frac{\xi_0}{2d_f} \right) T_{c0}, \quad (\text{S9})$$

where C_{Curie} is the Curie constant in the paraelectric phase and factor 2 before d_f corresponds to the mentioned effective thickness doubling. The inverse scaling of the renormalized transition temperature with ferroelectric layer thickness, d_f , allows us to sketch the temperature-thickness phase diagram of the system, presented in panel (b) where we distinguish four typical regions for states with distinct dielectric and ferroelectric properties, depicted in panel (c). The dependencies of the average polarizations, dielectric constants and capacitancies for the ferroelectric layers of different thickness on the temperature are shown in panels (d-f) respectively.

I. Paraelectric state at $T > T_{c0}$. The system stays at the paraelectric state with the positive dielectric constant ϵ_p , hence capacitance C_p is



Supplementary Figure 5 | Negative capacitance of the disc-shape ferroelectric layer in MFMS FET **a**, Vertical and horizontal cross-sections of the MFMS FET. At the zero gate voltage $V = 0$ (left side), the equilibrium location of the DW is in the middle of the ferroelectric disc. At the finite applied voltage, $V = V_g$, the DW displaces from the middle and bends (right side). **b**, The charge-voltage characteristics, $V_f(Q_f)$, of the disc-shape ferroelectric layer in MFMS FET. The monodomain and two-domain operational regions are displayed as turquoise and purple, respectively, inter-shaded regions. The threshold charges $\pm Q_f^*$ at which the domain wall leaves the ferroelectric nanodot mark the transition from the negative capacitance two-domain region to the positive capacitance monodomain region.

given by the Curie relation

$$C_p = \epsilon_0 \epsilon_p \frac{S_f}{d_f}, \quad \epsilon_p = \frac{C_{\text{Curie}}}{T - T_{c0}} + \epsilon_i. \quad (\text{S10})$$

II. Incipient ferroelectric state [5] existing at $T_{c0} > T > T_{cm}$. This state precedes the transition to the multidomain ferroelectric state, however, the system maintains the paraelectric phase with $P = 0$ at $V_g = 0$. Importantly, the value of the dielectric constant is still given by the relation (S10). After passing through the pole at T_{c0} , the dielectric constant becomes negative and decreasing by its absolute value from infinity at T_{c0} to the minimal possible (for the incipient state) value at T_{cm} [24, 25]. That is why, the incipient state is also considered as a potential state for realizing the NC FET [25]. The origin of the NC in the incipient state is the specific arrangement of the depolarization charges at the FS interface, that inverts the induced intrinsic field within the ferroelectric layer oppositely to the applied voltage. The corresponding NC, calculated at T_{cm} is:

$$C_{\text{ins}} \approx -\epsilon_0 \frac{S_f}{d_f} \frac{1}{\pi} \left(\epsilon_{\perp} \frac{C_{\text{Curie}}}{T_{c0}} \right)^{1/2} \frac{\xi_0}{d_f}. \quad (\text{S11})$$

III. Soft multidomain ferroelectric state emerging at $T \leq T_{cm}$. The domain structure, shown in panel (g) has a gradual periodic polarization profile composed of the spontaneous z -component $P_z \sim \cos \frac{\pi z}{2d_f} \cos \frac{\pi x}{w}$ and the depolarization-field induced component, that in the soft-domain state has, preferably, the x orientation $P_x = -\epsilon_0 (\epsilon_{\perp} - 1) \partial_x \varphi \sim \sin \frac{\pi z}{2d_f} \sin \frac{\pi x}{w}$. Here the coordinate axis x and z are selected along and across the ferroelectric layer with the origin at the FM interface and the depolarization potential is given by Poisson equation: $\epsilon_0 \epsilon_{\perp} \partial_x^2 \varphi + \epsilon_0 \epsilon_i \partial_z^2 \varphi = \partial_z P_z$. The overall soft polarization profile, appearing as a superposition of the spontaneous and field-induced components, $\mathbf{P} = (P_x, P_z)$, (see panel (g)) is seen in experiment as a periodic vortex-antivortex texture and was also dubbed as a vortex phase [38]. The negative capacitance in the soft-domain phase is provided by the dominant phase volume of wide domain-wall regions [18] having the locally negative dielectric constant [5]. Its absolute value continues to slightly decrease, see also Refs. [19, 21, 24] for the interpolation formulas.

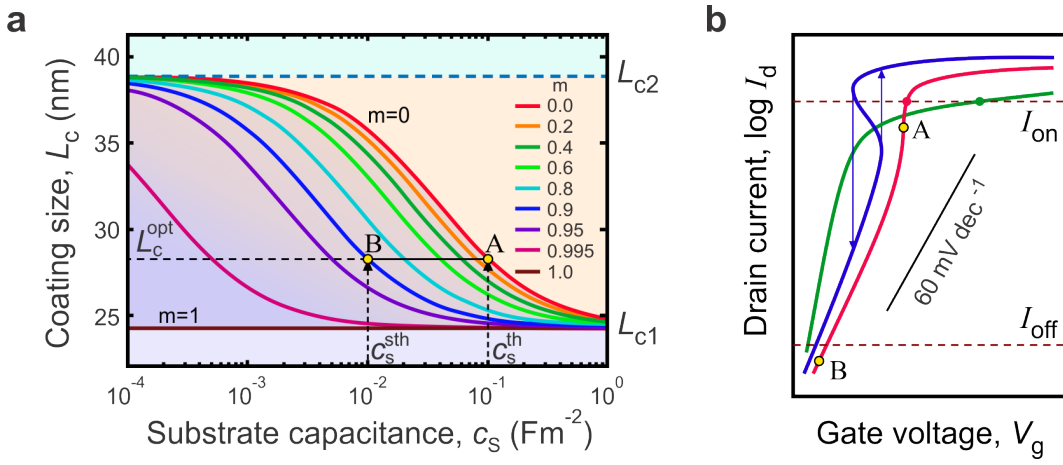
IV. Hard multidomain ferroelectric state, stabilizing below crossover temperature at $T_m^* < T_{cm}$ with the Landau-Kittel like flat-polarization domain profile. The mechanism of NC is mostly provided by the field-induced motion of domain walls [22]. Although this regime is not fully reachable in the nanometer-thin films (see phase diagram at panel (b)), the respective value of capacitance, $C_m < 0$, given in Supplementary Note 1, can be considered as the lower bound for the absolute value of NC of ferroelectric layer in MFS and MFIS FETs.

Figure S4 demonstrates the distribution of the polarization and electric field in the MFS FET with the $d_f = 8$ nm thick ferroelectric layer at room temperature, the voltage applied at the gate being $V_g = 1$ V. The FS interface and the region of induced conducting channel, spaced from the interface on δ , are shown by the solid and dashed blue lines, respectively. Importantly, the nonuniform distribution of polarization in the ferroelectric, shown in panel (a) induces the nonuniform distribution of the electric field and potential (panels (b) and (c)) that penetrate into the semiconductor over the penetration depth $\sim w$. Therefore, the distribution of the depolarization electric potential in the channel region, $\varphi_s \sim \cos \frac{\pi x}{w} e^{-\pi \delta / w}$, is highly nonuniform. The characteristic variation of φ_s in the near-channel region ~ 1.2 V, shown in panel (d) by the potential line scattering is remarkably big. Not only it does exceed the voltage gain in the near-channel region ~ 0.3 V due to ferroelectric NC, shown by the read line, but is also comparable with the transistor operation voltage. This strong nonuniformity of the field makes the conducting channel inoperable. It also implies that the suggestion to introduce the buffer dielectric layer in between the ferroelectric and semiconducting layers to attenuate the field oscillations, making thus the MFIS configuration, will barely improve the situation. As it is clear from the plots of panel (d), the damping of the field nonuniformity occurs at the distances $> w$ where the NC potential amplification effect is not actual anymore.

Another problem related to the realization of the MFS FET, is the very big absolute value of the surface-normalized NC of the ferroelectric gate, c_{NC} , which, typically, does not go below 0.6 F m^{-2} , see Fig. S3, which substantially exceeds the capacitance of semiconducting substrate $c_s \sim 0.01 \text{ F m}^{-2}$. Such a relation between c_{NC} and c_s does not allow to achieve the visible gain in the amplification of the input voltage in the channel region since the decreasing body factor below $m = 1$ is very small, as it is shown at the same panel. This problem is especially pertinent for the attempts to realize the NC in the incipient regime, which is seemingly attractive due to the homogeneous distribution of the electric potential in the region of the conducting channel. However, at these parameters the body factor is not going to reduce below 0.99 [25], as can be also estimated from the formula (S11) which, together with the difficulty in achieving the proper temperature regime, makes the idea unpractical.

Supplementary Note 5: c-MFMS FET: Negative capacitance and practical design

Why the capacitance of the MFM capacitor is negative? Shown in Fig. S5 are the vertical and horizontal cross-sections of a nanoscale ferroelectric disc-shape MFM capacitor integrated in the MFMS FET, and demonstration of how manipulating with the DW position leads to NC. At the zero charge Q_f at the electrodes of the ferroelectric capacitor, corresponding to the zero voltage at the transistor, the DW sits in the



Supplementary Figure 6 | Determination of the optimal parameters for the gate-substrate match. **a**, A set of $L_c(c_s)$ dependencies. The arrows define a procedure for selecting the optimal coating size L_c^{opt} providing the best performance and stability of the transistor. **b**, Transport characteristics $I_d(V_g)$ of representative c-MFMIS FETs. The red curve shows $I_d(V_g)$ for optimally designed c-MFMIS FET. The green and blue curves show the $I_d(V_g)$ dependencies for transistors with the steeper SS having the voltage-independent (green) and nonlinear in voltage (blue, with hysteresis) substrate capacitancies.

middle of the disc, see left hand side of panel (a). The intrinsic charges at the respective electrodes redistribute in order to compensate the depolarization charges of each domain (keeping the total charge $Q_f = 0$) and to banish the electric field inside the ferroelectric disc, reducing thus the electrostatic energy. The finite charge Q_f , induced by the voltage $V = V_g$ applied to the transistor gate, displaces the DW from the middle zero-voltage position, see right hand side of panels (a). Accordingly, the intrinsic charges rearrange (maintaining the total charge Q_f) to compensate the depolarization fields of now unequal domains. Remarkably, when moving apart from the middle, the DW not only compensates the electric field arising due to the charge transferred to the electrodes but, minimising its surface self-energy, shrinks in the width w and bends because of the cylinder shape of a ferroelectric. As a result, the DW overshoots towards the edge beyond the electrostatics-demanded equilibrium position at which the internal electric field would have disappeared. Hence the net electric field not just vanishes to zero but flips over, emerging to go from the negatively charged electrode to the positively charged electrode, which expresses the negative capacitance. Quantitative description of the effect is given in Ref. [23].

Minimal gate model. In order to properly integrate the coated two-domain c-MFMI gate into the industrial design of the NC FET we need to elaborate on the minimal model, describing the Q_g - V_g characteristics of the gate that needs to be incorporated into the circuit simulator package. In the low-voltage and low-charge operational mode of the NC FET this model is defined by the linear relation $Q_g = C_g V_g$, where C_g is given by Eqs. (2) and (3) of the main text. Looking forward to extensive applications of our model for description of the c-MFMIS FET, we expand the model's working range beyond the non-linearity regime where substantial shifts of the domain wall and even its escape from the sample may occur.

The complete set of the Q_g - V_g characteristics of the gate is defined by the individual electric properties of its components, including the gate dielectric capacitor, coating capacitor and ferroelectric capacitor which form the equivalent circuit shown in Fig. 1f of the main text and which are characterized by the linear, $V_d = C_d^{-1} Q_d$, $V_c = C_c^{-1} Q_c$, and nonlinear, $V_f = V_f(Q_f)$, constituent relations respectively.

For the practical purposes, the V_g - Q_g characteristics can be parametrically plotted as functions of the running parameter Q_f , using the equations

$$\begin{aligned} V_g &= \left(1 + \frac{C_c}{C_d}\right) V_f(Q_f) + \frac{Q_f}{C_d} \\ Q_g &= C_c V_f(Q_f) + Q_f \end{aligned} \quad (\text{S12})$$

based on the relations $Q_g = Q_d = Q_c + Q_f$, $V_g = V_d + V_f$, and $V_f = V_d$ for the circuit in Fig. 1f of the main text.

The nonlinear constitutive relation, $V_f = V_f(Q_f)$, of the ferroelectric capacitor is the core relation that defines different regimes of the gate functioning. Shown in the Fig. S1b phase-field simulations of Q_f - V_f characteristics of ferroelectric capacitors reveal two different operational modes: the NC low-charge branch, $V_2(Q_f)$, (red curve) corresponding to the two-domain state where the domain wall motion is responsible for the electric properties of capacitor, and the high-charge branch, $V_1(Q_f)$, with the positive differential capacitance, $C_f = dV/dQ > 0$ (upper and lower segments of the blue curve), where the domain wall is gone and the capacitor falls into the monodomain state. Therefore, in total, the Q_f - V_f characteristics of the ferroelectric capacitor is presented by the synthetic dependence

$$V_f(Q_f) = \begin{cases} V_2(Q_f) & \text{if } |Q_f| < Q_f^* \\ V_1(Q_f) & \text{if } |Q_f| > Q_f^* \end{cases} \quad (\text{S13})$$

where Q_f^* is the charge at which the branches $V_2(Q_f)$ and $V_1(Q_f)$ meet.

To implement the $V_f(Q_f)$ function in the circuit simulator package, one should use the stable parts of the GL monodomain characteristics, described in Supplementary Note 2 for $V_1(Q_f)$. For the $V_2(Q_f)$ function it is convenient to use the analytical model for the two-domain ferroelectric capacitor [23] in which.

$$V_2(Q_f) = -\frac{Q_f}{C_f} \psi\left(\frac{Q_f}{s_f P_0}\right) D, \quad 8\gamma/\pi \approx 0.25 \quad (\text{S14})$$

where $\psi(s)$ ($0 < s < 1$), defined in Ref. [23], is the function accounting for the geometry of the system and conventionally approximated by the relation

$$\begin{aligned} \psi(s) &= (32/3\pi^2) \left[1.0 - 0.027s - 0.95s^2 - 0.34s^3 + 0.32s^4\right]^{1/2}, \\ 32/3\pi^2 &\approx 1.08 \end{aligned} \quad (\text{S15})$$

(In the linear in Q_f approximation, when $s \rightarrow 0$, Eq. (S14) gives C_{NC} in Eq. (3) of the main text that corresponds to C_2 in Supplementary Table I.) The plot of the analytical expression for the charge-voltage characteristics of the two-domain branch of the ferroelectric capacitor is presented in Fig. S3 for the parameters given above by the red dashed curve. The plot of the overall $V_f(Q_f)$ function describing the minimal model of the ferroelectric capacitor in two- and monodomain operational regimes is shown in Fig. S5. In general, the described minimal model provides a satisfactory approximation and holds in the wide range of the system parameters.

Optimal match between gate and substrate. Here we consider how to optimize the system parameter and match the capacitancies of the gate and substrate to ensure the best performance of the system. The emerging challenge here is the complex and highly nonlinear nature of C_s comprising contributions from the depletion layer capacitance, from the conducting carriers leading to the so-called quantum capacitance, from the interface charges, and from the source/drain geometrical capacitancies [9]. While being of a relatively low value, coming mainly from the capacitance of the depletion layer in the low-conducting regime at small voltages, C_s increases dramatically, typically by order of magnitude, due to the injection of conducting electrons into the channel caused by the gate bias near and above threshold value.

Using the $L_c(c_s, m)$ curves, see the main text, Fig. 2e, which we copy here as Fig. S6a, enables us to determine the optimal match between the NC gate capacitance and the semiconducting substrate capacitance ensuring the best-performance SS and stability of the transistor. To exemplify the nonlinear behaviour of the substrate we take the normalized capacitance $c_s^{\text{sth}} \approx 10^{-2} \text{ Fm}^{-2}$ in the low-voltage subthreshold regime and $c_s^{\text{th}} \approx 10^{-1} \text{ Fm}^{-2}$ in the high-voltage near-threshold regime. Next, we set the condition $m = 0$ at the steepest point of the $I(V_g)$ curve, i.e. in the near-threshold gate voltage where $c_s = c_s^{\text{th}}$. This condition, visualized by the point A in Fig. S6a, provides us with the optimal value of the size of the coating layer, $L_c^{\text{opt}} \approx 28 \text{ nm}$. Decreasing the gate voltage V_g to subthreshold values, reduces c_s and moves it to the left from the point A along the black line until reaching the point B corresponding to $c_s = c_s^{\text{sth}}$ at $V_g \approx 0$. The body factor at the point B is $m = 0.9$ which gives $SS \approx 0.54 \text{ mV dec}^{-1}$.

The corresponding transfer characteristic $I_d(V_g)$ is sketched in Fig. S6b (that is the copy of the Fig. 2f of the main text) by the red curve. It starts with the relatively modest $SS \approx 0.54 \text{ mV dec}^{-1}$ but steepens upon the increase in V_g , reaching its steepest value of about zero mV dec^{-1} in the near-threshold region. The location of points A and B corresponds to the capacitancies c_s^{th} and c_s^{sth} of panel (a). Because of the nonlinearity of c_s , the transfer characteristics of the designed c-MFMIS FET with $L_c = L_c^{\text{opt}}$ demonstrates the better performance at the same on-off current switching ratio, $I_{\text{on}}/I_{\text{off}}$, than the shown by the green curve commonly assumed NC FET with the voltage-independent substrate capacitance c_s , although having the steeper initial SS . At the same time, an attempt to engineer the NC FET having the nonlinear c_s with an initially steeper SS (exemplified by the blue curve), results in the hysteresis instability in switching. These considerations constitute the basis for the conceptual design of the bulk c-MFMIS FET.

Acknowledgements

This work was supported by H2020 RISE-MELON action (I.L.), and by Terra Quantum AG (I.L., A.R., and V.M.V.).

References

- Horowitz, M. *et al.* *Scaling, power, and the future of CMOS in IEEE International Electron Devices Meeting, 2005. IEDM Technical Digest.* (2005), 7–15.
- Salahuddin, S. & Datta, S. Use of negative capacitance to provide voltage amplification for low power nanoscale devices. *Nano Lett.* **8**, 405–410 (2008).
- Tu, L., Wang, X., Wang, J., Meng, X. & Chu, J. Ferroelectric negative capacitance field effect transistor. *Adv. Electron. Mater.* **4**, 1800231 (2018).
- Kobayashi, M. A perspective on steep-subthreshold-slope negative-capacitance field-effect transistor. *Appl. Phys. Express* **11**, 110101 (2018).
- Íñiguez, J., Zubko, P., Luk'yanchuk, I. & Cano, A. Ferroelectric negative capacitance. *Nat. Rev. Mater.* **4**, 243–256 (2019).
- Hoffmann, M. *et al.* Unveiling the double-well energy landscape in a ferroelectric layer. *Nature* **565**, 464–467 (2019).
- Alam, M. A., Si, M. & Ye, P. D. A critical review of recent progress on negative capacitance field-effect transistors. *Appl. Phys. Lett.* **114**, 090401 (2019).
- Bacharach, J., Ullah, M. S. & Fouad, E. *A Review on Negative Capacitance Based Transistors in 2019 IEEE 62nd International Midwest Symposium on Circuits and Systems (MWSCAS)* (2019), 180–184.
- Cao, W. & Banerjee, K. Is negative capacitance FET a steep-slope logic switch? *Nat. Commun.* **11**, 1–8 (2020).

- Hoffmann, M., Slesazek, S. & Mikolajick, T. Progress and future prospects of negative capacitance electronics: A materials perspective. *APL Mater.* **9**, 020902 (2021).
- Mikolajick, T. *et al.* Next generation ferroelectric materials for semiconductor process integration and their applications. *Journal of Applied Physics* **129**, 100901 (2021).
- Khosla, R. & Sharma, S. K. Integration of Ferroelectric Materials: An Ultimate Solution for Next-Generation Computing and Storage Devices. *ACS Applied Electronic Materials* (2021).
- Hoffmann, M., Slesazek, S., Schroeder, U. & Mikolajick, T. What's next for negative capacitance electronics? *Nat. Electron.* **3**, 504–506 (2020).
- Rethinking negative capacitance research. *Nat. Electron.* **3**, 503 (2020).
- Landauer, R. Can capacitance be negative? *Collective Phenomena* **2**, 167–170 (1976).
- Bratkovsky, A. & Levanyuk, A. Abrupt appearance of the domain pattern and fatigue of thin ferroelectric films. *Phys. Rev. Lett.* **84**, 3177–3180 (2000).
- Stephanovich, V., Luk'yanchuk, I. & Karkut, M. Domain-enhanced inter-layer coupling in ferroelectric/paraelectric superlattices. *Phys. Rev. Lett.* **94**, 047601 (2005).
- De Guerville, F., Luk'yanchuk, I., Lahoche, L. & El Marssi, M. Modeling of ferroelectric domains in thin films and superlattices. *Mat. Sci. Eng. B* **120**, 16–20 (2005).
- Luk'yanchuk, I. A., Lahoche, L. & Sené, A. Universal properties of ferroelectric domains. *Phys. Rev. Lett.* **102**, 147601 (2009).
- Zubko, P., Stucki, N., Lichtensteiger, C. & Triscone, J.-M. X-ray diffraction studies of 180° ferroelectric domains in PbTiO₃/SrTiO₃ superlattices under an applied electric field. *Phys. Rev. Lett.* **104**, 187601 (2010).
- Zubko, P. *et al.* Negative capacitance in multidomain ferroelectric superlattices. *Nature* **534**, 524–528 (2016).
- Luk'yanchuk, I., Sené, A. & Vinokur, V. M. Electrostatics of ferroelectric films with negative capacitance. *Phys. Rev. B* **98**, 024107 (2018).
- Luk'yanchuk, I., Tikhonov, Y., Sené, A., Razumnyaya, A. & Vinokur, V. Harnessing ferroelectric domains for negative capacitance. *Commun. Phys.* **2**, 22 (2019).
- Sené, A. *Théorie des domaines et des textures non uniformes dans les ferroélectriques* PhD thesis (Université de Picardie Jules Verne, 2010). <https://tel.archives-ouvertes.fr/tel-01344584>.
- Cano, A. & Jiménez, D. Multidomain ferroelectricity as a limiting factor for voltage amplification in ferroelectric field-effect transistors. *Appl. Phys. Lett.* **97**, 133509 (2010).
- Hoffmann, M., Pešić, M., Slesazek, S., Schroeder, U. & Mikolajick, T. On the stabilization of ferroelectric negative capacitance in nanoscale devices. *Nanoscale* **10**, 10891–10899 (2018).
- Khan, A. I., Radhakrishna, U., Chatterjee, K., Salahuddin, S. & Antoniadis, D. A. Negative capacitance behavior in a leaky ferroelectric. *IEEE Transactions on Electron Devices* **63**, 4416–4422 (2016).
- Hasler, P., Minch, B. A. & Diorio, C. An autozeroing floating-gate amplifier. *IEEE Trans. Circuits Syst. II-Analog Digit. Signal Process.* **48**, 74–82 (2001).
- Kotani, K., Shibata, T., Imai, M. & Ohmi, T. Clock-controlled neuron-MOS logic gates. *IEEE Trans. Circuits Syst. II-Analog Digit. Signal Process.* **45**, 518–522 (1998).
- Pertsev, N., Zembilgotov, A. & Tagantsev, A. Effect of mechanical boundary conditions on phase diagrams of epitaxial ferroelectric thin films. *Phys. Rev. Lett.* **80**, 1988 (1998).
- Logg, A., Mardal, K.-A., Wells, G. N., *et al.* *Automated Solution of Differential Equations by the Finite Element Method* ISBN: 978-3-642-23098-1 (Springer, 2012).
- Tikhonov, Y., Kondovych, S., Mangeri, J., *et al.* Controllable skyrmion chirality in ferroelectrics. *Sci. Rep.* **10**, 8657 (2020).
- Geuzaine, C. & Remacle, J.-F. Gmsh: A three-dimensional finite element mesh generator with built-in pre- and post-processing facilities. *Int. J. Numer. Methods Eng.* **79**, 1039–1331 (2009).
- Loring, B., Karimabadi, H. & Rortershteyn, V. *A Screen Space GPGPU Surface LIC Algorithm for Distributed Memory Data Parallel Sort Last Rendering Infrastructures in Numerical Modeling of Space Plasma Flows ASTRONUM-2014* (eds Pogorelov, N. V., Audit, E. & Zank, G. P.) **498** (Oct. 2015), 231.
- Janelli, A. & Fazio, R. Adaptive stiff solvers at low accuracy and complexity. *J. Comput. Appl. Math.* **191**, 246 (2006).
- Balay, S. *et al.* *PETSc Web page* <https://www.mcs.anl.gov/petsc>. 2021. <https://www.mcs.anl.gov/petsc>.
- Balay, S. *et al.* *PETSc Users Manual* tech. rep. ANL-95/11 - Revision 3.15 (Argonne National Laboratory, 2021). <https://www.mcs.anl.gov/petsc>.
- Yadav, A. *et al.* Observation of polar vortices in oxide superlattices. *Nature* **530**, 198–201 (2016).